CHALMERS
UNIVERSITY OF TECHNOLOGY

Detection of vibrationally excited HC7N and HC9N in IRC+10216

A&A 640, L13 (2020)
https://doi.org/10.1051/0004-6361/202038571

Astronomy & Astrophysics

LETTER TO THE EDITOR

Detection of vibrationally excited HC_7N and HC_9N in IRC +10216★

J. R. Pardo[1], C. Bermúdez[1], C. Cabezas[1], M. Agúndez[1], J. D. Gallego[2], J. P. Fonfría[1], L. Velilla-Prieto[1,3], G. Quintana-Lacaci[1], B. Tercero[2,4], M. Guélin[5], and J. Cernicharo[1]

[1] Grupo de Astrofísica Molecular, Instituto de Física Fundamental (IFF-CSIC), C/ Serrano 121, 28006 Madrid, Spain
e-mail: jose.cernicharo@csic.es
[2] Centro de Desarrollos Tecnológicos, Observatorio de Yebes (IGN), 19141 Yebes, Guadalajara, Spain
[3] Department of Space, Earth and Environment, Chalmers University of Technology, Onsala Space Observatory, 439 92 Onsala, Sweden
[4] Observatorio Astronómico Nacional (OAN, IGN), Madrid, Spain
[5] Institut de Radioastronomie Millimétrique, 300 Rue de la Piscine, 38406 Saint Martin d'Hères, France

Received 3 June 2020 / Accepted 29 June 2020

ABSTRACT

Observations of IRC +10216 with the Yebes 40 m telescope between 31 and 50 GHz have revealed more than 150 unidentified lines. Some of them can be grouped into a new series of 26 doublets, harmonically related with integer quantum numbers ranging from J_{up} = 54 to 80. The separation of the doublets increases systematically with J, that is to say, as expected for a linear species in one of its bending modes. The rotational parameters resulting from the fit to these data are B = 290.8844 ± 0.0004 MHz, D = 0.88 ± 0.04 Hz, and q = 0.1463 ± 0.0001 MHz. The rotational constant is very close to that of the ground state of HC_9N. Our ab initio calculations show an excellent agreement between these parameters and those predicted for the lowest energy vibrationally excited state, v_{19} = 1, of HC_9N. This is the first detection, and complete characterization in space, of vibrationally excited HC_9N. An energy of 41.5 cm^{-1} is estimated for the v_{19} state. In addition, 17 doublets of HC_7N in the v_{15} = 1 state, for which laboratory spectroscopy is available, were detected for the first time in IRC +10216. Several doublets of HC_5N in its v_{11} = 1 state were also observed. The column density ratio between the ground and the lowest excited vibrational states are ≈127, 9.5, and 1.5 for HC_5N, HC_7N, and HC_9N, respectively. We find that these lowest-lying vibrational states are most probably populated via infrared pumping to vibrationally excited states lying at ≈600 cm^{-1}. The lowest vibrationally excited states thus need to be taken into account to precisely determine absolute abundances and abundance ratios for long carbon chains. The abundance ratios $N(HC_5N)/N(HC_7N)$ and $N(HC_7N)/N(HC_9N)$ are 2.4 and 7.7, respectively.

Key words. molecular data – line: identification – stars: carbon – circumstellar matter – stars: individual: IRC +10216 – astrochemistry

1. Introduction

Sensitive line surveys are the best tool to unveil the molecular content of astronomical sources and to search for new molecules. A key element for carrying out a detailed analysis of line surveys is the availability of spectroscopic information of the already-known species, their isotopologues, and their vibrationally excited states. The ability to identify the maximum possible number of lines coming from them leaves the cleanest possible forest of unidentified lines; this opens up a chance to discover new molecules and to get insights into the chemistry and chemical evolution of the observed object. Lines from vibrationally excited states of long molecules have been observed in the carbon-rich circumstellar envelope (CSE) IRC +10216; C_4H and C_6H are good examples of such emission (Guélin et al. 1993; Yamamoto et al. 1987; Cernicharo et al. 2008). The longer a linear molecule is, the lower in energy its vibrational bending modes are. Hence, even in relatively cold regions of CSEs, the lines from vibrationally excited states can be rather prominent in sensitive surveys. Moreover, the correct determination of the abundance ratios between species of the same family (e.g. C_nH radicals or cyanopolyynes $HC_{2n+1}N$) requires an estimation of populations in vibrationally excited states if they are significant.

Rotational lines from vibrationally excited levels of moderate energies provide useful information on the pumping mechanisms in the CSE and allow us to assess the role of infrared (IR) pumping and its effect on intensity line variations with the stellar phase (Cernicharo et al. 2008, 2014; Agúndez et al. 2017; Pardo et al. 2018). A different case occurs when these lines involve very high energy vibrational states because they trace the physical and chemical conditions of the innermost and warm regions of CSEs. The main difference between the rotational lines from low and high energy vibrational states relies on the line profile. Transitions from low energy excited vibrational levels should show the same velocity extent and similar line profiles as those of the ground vibrational state, with C_4H and C_6H as clear examples (Guélin et al. 1993; Cernicharo et al. 2008). However, rotational lines from high energy excited vibrational states show Gaussian profiles and trace the kinematics of the gas in the innermost regions (Cernicharo et al. 2011, 2013; Patel et al. 2011).

★ Based on observations carried out with the Yebes 40 m telescope and the IRAM 30 m telescope. The 40 m radiotelescope at Yebes Observatory is operated by the Spanish Geographic Institute (IGN, Ministerio de Transportes, Movilidad y Agenda Urbana). IRAM is supported by INSU/CNRS (France), MPG (Germany), and IGN (Spain).

In this Letter we report on the discovery of a new series of lines toward IRC +10216 that we attribute to the $\nu_{19} = 1$ state of HC_9N, for which we determine accurate rotational constants. In addition, we report on the detection of HC_7N in the $\nu_{15} = 1$ and $\nu_{15} = 2$ states, and of HC_5N in the $\nu_{11} = 1$ state. The abundance ratio between members of this molecular family is revisited in the light of the high column densities observed in vibrationally excited states for some of them.

2. Observations

The Q-band observations (31.0–50.3 GHz) were carried out in spring 2019 with the 40 m radiotelescope of the Centro Astronómico de Yebes (IGN, Spain), hereafter Yebes 40 m. New receivers, built within the Nanocosmos project[1] and installed at the telescope, were used for these observations during its commissioning phase. The experimental setup will be described elsewhere (Tercero et al., in prep.). Briefly, the Q-band receiver consists of two HEMT cold amplifiers covering the 31.0–50.3 GHz band with horizontal and vertical polarizations. Receiver temperatures vary from 22 K at 32 GHz to 42 K at 50 GHz. The backends are 16 × 2.5 GHz fast Fourier transform spectrometers (FFTS) with a spectral resolution of 38.1 kHz providing the whole coverage of the Q-band in both polarizations. The observing mode was position switching with an off position at 300″ in azimuth. The main beam efficiency varies from 0.6 at 32 GHz to 0.43 at 50 GHz. The spectra were smoothed to a resolution of 0.195 MHz, that is, a velocity resolution of ≈1.9 and 1.2 km s^{-1} at 31 and 50 GHz, respectively. The sensitivity of the final spectra varies from 0.4 to 1 mK across the Q-band, which is a factor of ≈10 better than previous observations in the same band made with the Nobeyama 45 m telescope (Kawaguchi et al. 1995).

The observations in the λ3 mm band presented in this paper were carried out with the IRAM 30 m radio telescope and were described in detail by Cernicharo et al. (2019). Briefly, they correspond to observations acquired over the last 35 years and cover the 70–116 GHz domain with very high sensitivity (1–3 mK). Examples of these data can be found in Cernicharo et al. (2004, 2007, 2008, 2019) and Agúndez et al. (2008, 2014).

The beam size of the Yebes 40 m in the Q-band is in the range 36–56″, while that of the IRAM 30 m telescope in the 3 mm domain is 21–30″. Pointing corrections were obtained by observing strong nearby quasars and the SiO masers of R Leo. Pointing errors were always within 2–3″. The intensity scale, antenna temperature (T_A^*), was corrected for atmospheric absorption using the ATM package (Cernicharo 1985; Pardo et al. 2001). We adopted calibration uncertainties to be 10%. Additional uncertainties could arise from the line intensity fluctuation with time, induced by the variation of the stellar IR flux (Cernicharo et al. 2014; Pardo et al. 2018). All data were analyzed using the GILDAS package[2].

3. Results

One of the most surprising results from the line survey in the Q-band is the presence of bright lines from vibrationally excited states of C_4H, C_6H, HC_5N, and HC_7N, and of two series of doublets recently assigned by Cernicharo et al. (2019) to MgCCCN and MgCCCCH (see Fig. 1, where the bottom panel shows one of the MgCCCN doublets). Also, a new series of lines consisting of 26 doublets, with central frequencies in harmonic relation from $J = 54$ up to $J = 80$, was found in the Q-band data.

None of the frequencies of the new doublets could be identified in the public JPL (Pickett et al. 1998) or CDMS (Müller et al. 2005) catalogs or in the MADEX catalog (Cernicharo 2012). They belong to a new molecular species or to a new vibrationally excited state of a known molecule. The lines appear at frequencies slightly higher than those of HC_9N with the same quantum numbers. Line frequencies for this series of doublets were determined by fitting them with a specific line profile typical of expanding envelopes (Cernicharo et al. 2018). Selected lines of this series are shown in Figs. 1 and 2. The typical profile of the lines with rather sharp edges allows us to fit the lines' central frequencies with an accuracy on the order of, or even better than, the spectral resolution of the data, even when signals are weak (Cernicharo et al. 2018). Some doublets of this series are blended with other features, but frequencies can still be derived for most of them by fixing the expanding velocity to 14.5 km s^{-1} (Cernicharo et al. 2000, 2018). However, the integrated line intensities are rather uncertain in these cases. Observed and fitted line frequencies for these doublets are given in Table A.2. One of the components of the $J = 64–63$ doublet is fully blended with HC_7N $J = 33–32$, with a frequency difference between both features of ≈0.5 MHz. The other component of the same transition is blended with $HCCC^{13}CCN$ $J = 14 – 13$, with a frequency difference of 1.3 MHz. This is the only doublet missing in the series from $J = 54–53$ through $J = 80–79$.

The line frequencies were fitted to the following expression for the energy of the rotational levels in a excited vibrational bending mode with $\ell = 1$:

$$E(J, p) = B(J(J+1) - 1) - D(J(J+1) - 1)^2 \pm 1/2 q_t J(J+1), \quad (1)$$

where the sign ± corresponds to the different parities of each doublet (f for + and e for −, assuming q_t is positive following the convection of Brown et al. 1975) for a given value of J. Additional distortion terms were found unnecessary in the fitting process, the results of which are: $B = 290.8844 \pm 0.0003$ MHz, $D = 0.88 \pm 0.04$ Hz and $q_t = 0.1463 \pm 0.0001$ MHz, where the quoted uncertainties are 1 σ values. The standard deviation of the fit to the 52 observed lines is 105 kHz (roughly half a resolution element). The rotational constant, B, is just 0.37 MHz larger than that of the ground state of HC_9N, while the distortion constant, D, is practically the same: for the ground state of HC_9N, $B = 290.51832 \pm 0.00001$ MHz and $D = 0.860 \pm 0.010$ Hz (McCarthy et al. 2000). Hence, it is very likely that this series of doublets corresponds to a vibrational state of HC_9N with an excited bending mode. From the observed value of q_t and B, it is possible to estimate the frequency of this bending mode using the relation $\omega_\nu \approx 2.6\, B_\nu^2/q_{\nu t} \approx 50.1$ cm^{-1} (Gordy & Cook 1984). To assign the lines to one of the bending modes of HC_9N, we performed ab initio calculations at different levels of theory (see Appendix B). We unambiguously conclude that the lines belong to the lowest energy bending mode, $\nu_{19} = 1$, of HC_9N. From the observed rotational constants, we derive a first order vibration-rotation coupling constant $\alpha_{19} = -0.3661 \pm 0.0004$ MHz. Line intensities and other parameters for the observed HC_9N lines in the ground and its ν_{19} states are given in Table A.2.

For HC_5N, in addition to the lines of the ground vibrational state, all the doublets arising from its lowest vibrationally excited state ν_{11} were detected in the 31–50 and 70–116 GHz domains. It had previously been detected toward CRL 618 (Cernicharo et al. 2001; Wyrowski et al. 2003). Its energy above the ground state was estimated by Vichietti & Haiduke (2012) to be ≈111 cm^{-1} (see also Appendix B). Details on the available laboratory

[1] https://nanocosmos.iff.csic.es/
[2] http://www.iram.fr/IRAMFR/GILDAS

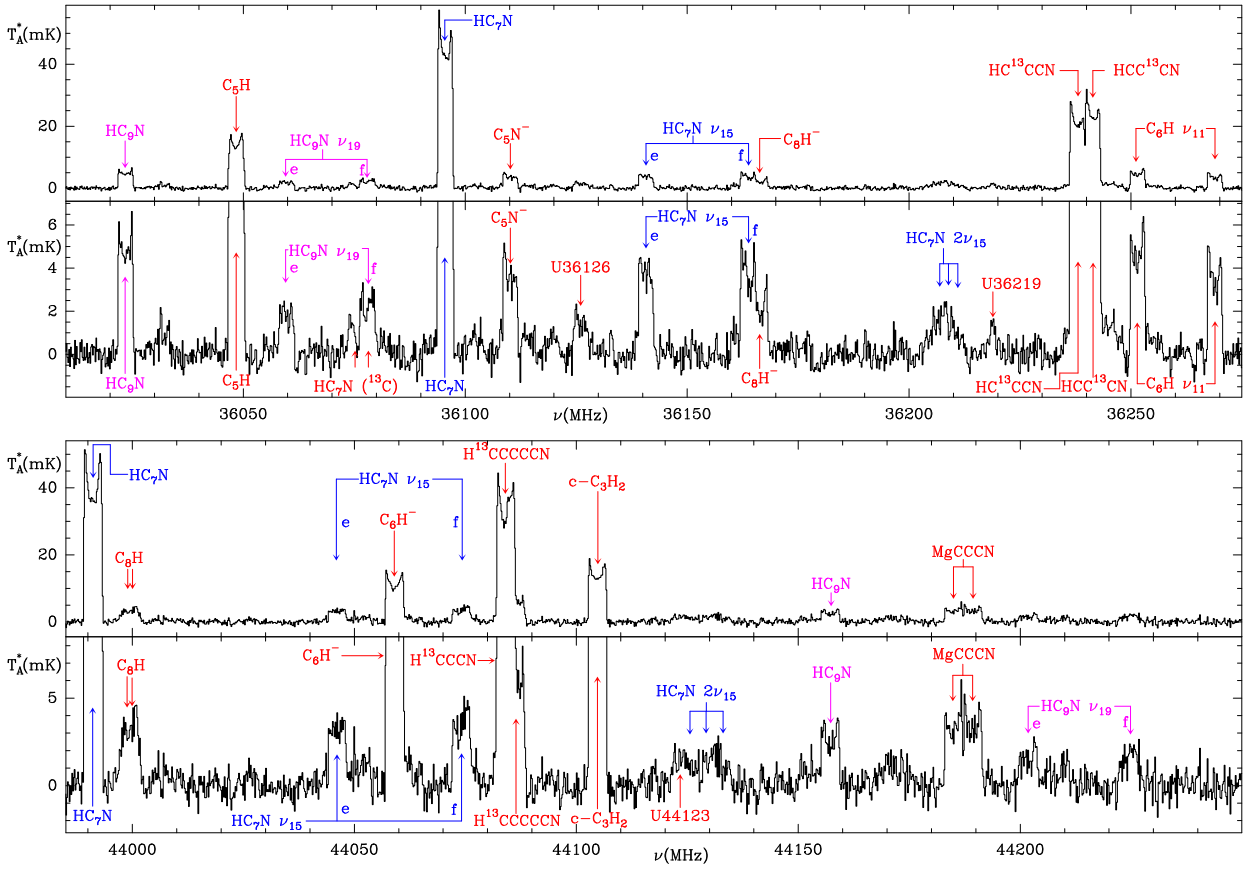

Fig. 1. Data from two frequency ranges within the *Q*-band observed with the Yebes 40 m telescope towards IRC +10216. Each frequency range is shown through two panels with different limits in intensity. The vertical scale is antenna temperature in mK. The horizontal scale is the rest frequency in MHz. Labels for HC_7N features are in blue, while those belonging to HC_9N are in violet. Other spectral features from known species, together with unidentified lines (labeled as "U" lines), are indicated in red. The $N = 16-15$ doublet of MgCCCN, a new species recently detected (Cernicharo et al. 2019), is shown in the bottom panels. Vibrationally excited lines from HC_7N, HC_9N, and C_6H are nicely detected at these frequencies. Additional lines from vibrationally excited states of HC_5N, HC_7N, and HC_9N are shown in Figs. 2, A.1, and A.3.

spectroscopy for this bending mode of HC_5N are given in Appendix A. Selected lines are shown in Fig. A.1, and the derived parameters are given in Table A.4.

For HC_7N, two series of lines from the v_{15} and $2v_{15}$ were detected in addition to those from the ground vibrational state. Figure 1 shows a couple of doublets from these two vibrationally excited states. Additional lines are shown in Fig. A.3. In the 70–116 GHz domain, only lines from the v_{15} state up to $J_{up} = 72$ were detected. Line parameters for HC_7N are given in Table A.3. This is the first time that this state has been analyzed in detail in space. Nevertheless, the v_{15} and $2v_{15}$ states are reported, but not discussed, in the figures in Pardo et al. (2004, 2008), Pardo & Cernicharo (2007). Several unidentified features in the 1.3 cm line survey of IRC +10216 by Gong et al. (2015) can also be assigned to the v_{15} state of HC_7N, namely U21458.8 ($J = 19-18e$), U23732.7 ($J = 21-20f$), U24862.7 ($J = 22-21f$), U25976.2, and U25992.8 ($J = 23-22e$ and f components).

4. Discussion

Vibrationally excited cyanopolyynes show a clear trend in which the line intensities, relative to those of the ground vibrational state, increase with increasing chain length. For HC_5N, the observed intensity ratio between the ground and the sum of the two components (e and f) of its $v_{11} = 1$ state is ≈30 (see Fig. A.1), while for HC_7N and its $v_{15} = 1$ state the ratio is ≈8, and for HC_9N and its $v_{19} = 1$ state it is ≈1. From the observed line shapes for these species, and taking into account the half power beam of the two telescopes, the emission arises from the external layers of the envelope where ultraviolet photons drive a rich photochemistry (Agúndez et al. 2017). The kinetic temperature in this zone of the CSE is ≈20-30 K (Agúndez et al. 2017). Hence, it is difficult to believe that the $v_{11} = 1$ state of HC_5N, which is at ≈160 K above the ground (Vichietti & Haiduke 2012), is pumped by collisions alone. The same applies to the $v_{15} = 1$ and $v_{19} = 1$ states of HC_7N and HC_9N, respectively, which lie at ≈92 K (Vichietti & Haiduke 2012) and ≈72 K (this work) above the ground. Pumping through IR photons coming from the internal regions of the envelope probably plays an important role in the excitation of these species.

We analyzed the HC_5N, HC_7N, and HC_9N data by constructing rotational diagrams for their ground and low-lying vibrational states. We assumed a 15″ radius for the source and convolved it with the main beam of both telescopes, depending on the line. For HC_9N, we find a rotational temperature for the $v_{19} = 1$ state very similar to that of the ground vibrational state, ≈23.5 K, and a column density ratio between the ground and the $v_{19} = 1$ state of 1.45 ± 0.50 (see Fig. 3). The vibrational partition function at 23.5 K (see Table A.1) is ≈1.15. If the $v_{19} = 1$ state is populated by collisions and thermalized with the ground state at this temperature, then its expected column density would be 8% that of the ground state. In fact, the derived vibrational temperature for the $v_{19} = 1$ is close to 80 K. Hence,

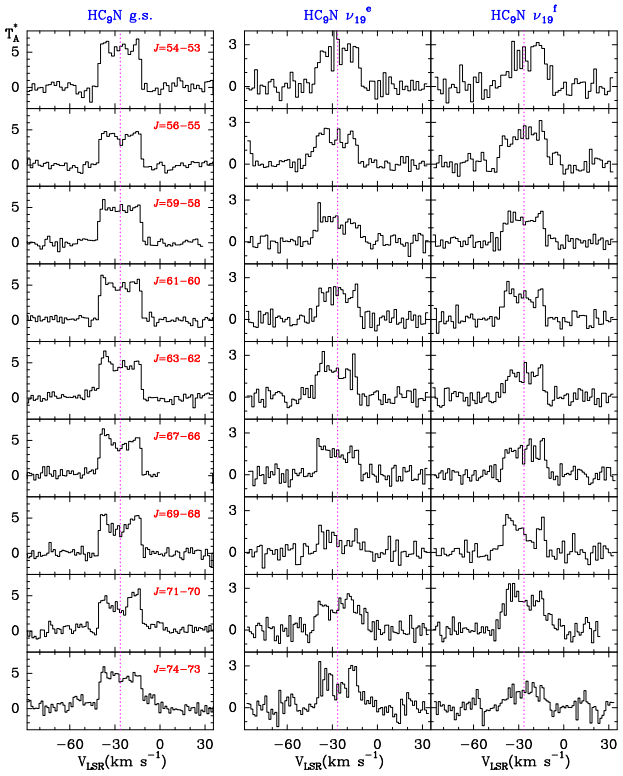

Fig. 2. Selected doublets of HC_9N ν_{19} = 1 in the 31–50 GHz domain. *Left panels*: lines of HC_9N in the ground vibrational state. The rotational quantum numbers are indicated in the top-right side of each panel. The same transitions for the ν_{19} = 1 state are shown in the middle (e component) and right (f component) panels. The intensity scale is antenna temperature in mK. The abscissa corresponds to local standard of rest (LSR) velocities in km s^{-1}. The vertical violet dotted line at −26.5 km s^{-1} indicates the systemic velocity of the envelope (Cernicharo et al. 2000, 2018). Two additional ν_{19} doublets are shown in Fig. 1.

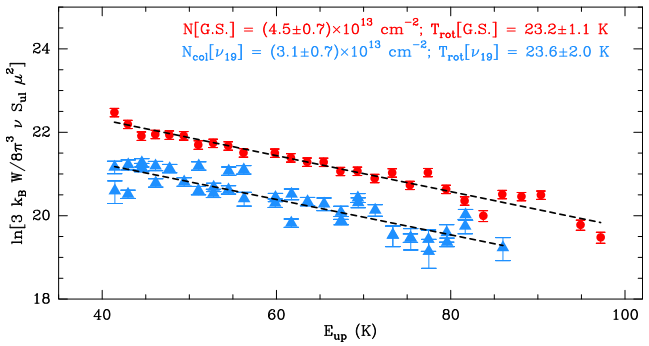

Fig. 3. Rotational diagram of HC_9N in its ground state (red) and ν_{19} = 1 vibrationally excited state (blue). The derived rotational temperatures and column densities are indicated in the plot.

an efficient mechanism must exist to pump molecules into this excited vibrational state. The column densities of HC_9N in the ground and the ν_{19} = 1 states are $(4.5 \pm 0.5) \times 10^{13}$ cm^{-2} and $(3.1 \pm 0.5) \times 10^{13}$ cm^{-2}, respectively. The total column density of this species is, hence, $(7.6 \pm 1.4) \times 10^{14}$ cm^{-2}. We searched for possible lines that could be assigned to the ν_{19} = 2 state without success. Hence, contribution from other vibrational levels is expected to be marginal.

For HC_5N and HC_7N, the rotational diagram analysis indicates the presence of a cold and a warm regime for the ground and the first vibrationally excited states (see Appendices A.1 and A.2). For these two components of HC_5N ($T_{\rm rot} \simeq$ 10 K and 25 K, respectively), we derive N(ground)/N(ν_{11} = 1) ≈ 127 and 93, respectively (see Appendix A.1). The total column density of HC_5N is thus $(8.3 \pm 0.7) \times 10^{14}$ cm^{-2}, with a negligible contribution of the ν_{11} state. For the cold ($T_{\rm rot} \simeq$ 17 K) and warm ($T_{\rm rot} \simeq$32 K) HC_7N components, we derive N(ground)/N(ν_{15} = 1) ≈ 9.5 and 1.5, respectively (see Appendix A.2). The total column density of HC_7N, including the contribution of its ν_{15} state, is $3.5 \pm 0.7 \times 10^{14}$ cm^{-2}. Hence, N(HC_5N)/N(HC_7N) ≃ 2.4 and N(HC_7N)/N(HC_9N) ≃ 7.7. The values obtained for these ratios by Gong et al. (2015), without any correction for the vibrational states, are 1.24 and 14.8, respectively. We note that without the contribution of the ν_{19} state, the abundance ratio N(HC_7N)/N(HC_9N) would be a factor of ≃2 higher. The trend in the total abundance ratio between consecutive cyanopolyynes is similar to that found in cold molecular clouds, ≃3–4; however, for long members of this molecular family, the low energy bending modes population can be as high as that of the ground state.

IR pumping for polyatomic molecules can proceed through different paths. Stretching and bending modes harbor a large number of states and bands that provide a plethora of radiative paths to pump the different levels of the molecule. The simple case of the triatomic molecule HNC, which has two stretching modes and one bending mode, was studied by Cernicharo et al. (2014). Excitation through each vibrational mode has a different effect on the line intensities of the ground vibrational state. In the case of HNC, the frequency of the bending mode is high and its IR intensity corresponds to large Einstein coefficients (i.e. the molecule in the bending mode decays mainly to the ground vibrational state). However, for long linear molecules, the frequencies of their bending modes and their IR intensities decrease with increasing chain length. Hence, Einstein coefficients of pure rotational transitions within the bending mode are similar to those of ro-vibrational transitions between the bending mode and the ground vibrational state. This allows for the maintenance of a significant population in the excited bending mode.

While in HNC there are a few radiative paths that redistribute the population of the ground vibrational state between the different vibrationally excited states, in the case of HC_9N there are ten stretching and nine bending modes. Hence, the number of transitions from the ground to excited vibrational states and the subsequent radiative de-excitation cascades is huge. Nevertheless, IR pumping will also depend on the flux of the source at the wavelengths of the different IR bands (see, e.g. Fonfría et al. 2008; Agúndez et al. 2017). In the case of IRC +10216, it is well known that the IR emission peaks around 10 μm (Cernicharo et al. 1999). Hence, we could expect to have a dominant path through vibrational bands with large IR intensities and frequencies around 1000 cm^{-1}.

To investigate these effects on the population of the excited vibrational states of cyanopolyynes in IRC +10216, we carried out excitation and radiative transfer calculations for HC_5N, HC_7N, and HC_9N. The physical structure of the envelope and the radial abundance profiles are taken from the chemical model of IRC +10216 from Agúndez et al. (2017). We consider rotational levels within the ground vibrational state, and also within the lowest-lying vibrational state (ν_{11} = 1 for HC_5N, ν_{15} = 1 for HC_7N, and ν_{19} = 1 for HC_9N). In addition, we include for each molecule rotational levels within a vibrational state associated with the CH bending mode (ν_7 = 1 for HC_5N, ν_9 = 1 for HC_7N, and ν_{11} = 1 for HC_9N), which has the most intense fundamental band at mid-IR wavelengths, where the radiation

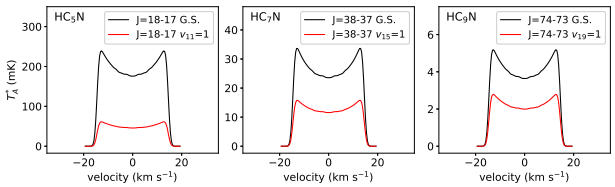

Fig. 4. Calculated line profiles for selected lines of HC_5N, HC_7N, and HC_9N in their ground state (G.S.) and lowest energy bending vibrational states. Calculated intensities have been multiplied by 10, 8, and 2 for HC_5N, HC_7N, and HC_9N, respectively, to match the observed intensities of the ground vibrational state lines.

field in IRC +10216 is high. We adopted the IR intensities calculated in this work at the second order Møller Plesset perturbation theory (MP2; Møller & Plesset 1934) in the anharmonic limit (see Table B.4). Since IR intensities between excited vibrational states are not known for these molecules, we assumed that molecules from the mid-IR-lying excited vibrational state decay to the lowest-lying vibrational state with the same Einstein coefficient as to the ground vibrational state. We note that this assumption is an important source of uncertainty in the models. We adopted the approximate expression of Deguchi & Uyemura (1984) as rate coefficients for pure rotational excitation through inelastic collisions with H_2. We considered ro-vibrational excitation through collisions to be negligible, an assumption that could introduce important uncertainties in the models due to the low energy separation between the rotational levels of the ground and the lowest-lying vibrational states. In summary, IR pumping occurs through absorption in the fundamental band of the CH bending mode, which lies around 600 cm^{-1} for the three cyanopolyynes, and through further radiative decay to the lowest-lying vibrational states and to the ground state.

In Fig. 4 we show the calculated line profiles for one selected rotational transition of HC_5N, HC_7N, and HC_9N lying in the Q-band in both the ground and the lowest-lying vibrational state. We see that the intensity of the line belonging to the lowest-lying vibrational state approaches the intensity of the line in the ground vibrational state as the size of the cyanopolyyne increases. The calculated line intensity ratio between the ground state and the lowest-lying vibrational state is ∼3.9, ∼2.2, and ∼1.9 for HC_5N, HC_7N, and HC_9N, respectively. These values differ from those observed. For example, they overestimate the relative population of the $\nu_{11} = 1$ state of HC_5N and the $\nu_{15} = 1$ state of HC_7N, although they agree reasonably well for the $\nu_{19} = 1$ state of HC_9N. In any case, the model satisfactorily reproduces the observed trend of increasing relative population of the vibrationally excited state with increasing molecular size.

The observed behavior in the abundance ratio of the cyanopolyynes could introduce an important limitation in detecting longer chains. While $HC_{11}N$ could be present in the envelope, its presence in space has never been confirmed (Cordiner et al. 2017). In our sensitive Q-band data, none of the expected transitions of the ground state are detected. Theoretical calculations of the vibrational modes of this species by Vichietti & Haiduke (2012) suggest that the lowest bending mode, ν_{23}, will be at an energy of 42 K. The effect of IR pumping could be very similar to that of HC_9N and would reduce the intensity of the rotational lines of the ground state by a factor of two. Hence, detecting $HC_{11}N$ would be at the sensitivity limit of present instruments. IR pumping also has important consequences on the possibility of detecting other long chain molecules, such as C_9H, $C_{10}H$, and $C_{11}H$. Their rotational frequencies are well known (see Gottlieb et al. 1998 and references therein). We have searched for them in our Q-band data without success. These species, as is the case for C_6H (Cernicharo et al. 2008), have very low energy bending modes that could be highly populated, decreasing the chances of detecting them in their ground vibrational states.

Acknowledgements. The Spanish authors thank Ministerio de Ciencia e Innovación for funding support through project AYA2016-75066-C2-1-P. We also thank ERC for funding through grant ERC-2013-Syg-610256-NANOCOSMOS. MA thanks Ministerio de Ciencia e Innovación for Ramón y Cajal grant RyC-2014-16277. CB thanks Ministerio de Ciencia e Innovación for Juan de la Cierva grant FJCI-2016-27983. LVP acknowledges support from the Swedish Research Council and from the ERC through the consolidator grant 614264.

References

Agúndez, M., Fonfría, J. P., Cernicharo, J., et al. 2008, A&A, 479, 493
Agúndez, M., Cernicharo, J., & Guélin, M. 2014, A&A, 570, A45
Agúndez, M., Cernicharo, J., Quintana-Lacaci, G., et al. 2017, A&A, 601, A4
Bizzocchi, L., Degli, Esposti C., & D., 2004, ApJ, 614, 518
Botschwina, P., Horn, M., Markey, M., & Oswald, R. 1997, Mol. Phys., 92, 381
Brown, J. M., Hougen, J. T., Huber, K.-P., et al. 1975, J. Mol. Spectrosc., 55, 500
Cernicharo, J. 1985, Internal IRAM Report (Granada: IRAM)
Cernicharo, J. 2012, in ECLA 2011: Proc. of the European Conference on Laboratory Astrophysics, eds. C. Stehl, C. Joblin, & L. d'Hendecourt (Cambridge: Cambridge Univ. Press), EAS Publ. Ser., 251, https://nanocosmos.iff.csic.es/?page_id=1619
Cernicharo, J., Yamamura, I., González-Alfonso, E., et al. 1999, ApJ, 526, L41
Cernicharo, J., Guélin, M., & Kahane, C. 2000, A&AS, 142, 181
Cernicharo, J., Heras, A. M., Pardo, J. R., et al. 2001, ApJ, 546, L127
Cernicharo, J., Guélin, M., & Pardo, J. R. 2004, ApJ, 615, L145
Cernicharo, J., Guélin, M., Agúndez, M., et al. 2007, A&A, 467, L37
Cernicharo, J., Guélin, M., Agúndez, M., et al. 2008, ApJ, 688, L83
Cernicharo, J., Agúndez, M., Kakane, C., et al. 2011, A&A, 529, L3
Cernicharo, J., Daniel, F., Castro-Carrizo, A., et al. 2013, ApJ, 778, L25
Cernicharo, J., Teyssier, D., Quintana-Lacaci, G., et al. 2014, ApJ, 796, L21
Cernicharo, J., Guélin, M., Agúndez, M., et al. 2018, A&A, 618, A4
Cernicharo, J., Cabezas, C., Pardo, J. R., et al. 2019, A&A, 630, L2
Cooksy, A. L., Gottlieb, C. A., Killian, T. C., et al. 2015, ApJS, 216, 30
Cordiner, M. A., Charnley, S. B., Kisiel, Z., et al. 2017, ApJ, 850, 187
Degli Esposti, C., Bizzocchi, L., Botschwina, P., et al. 2005, J. Mol. Spectrosc., 230, 185
Deguchi, S., & Uyemura, M. 1984, ApJ, 285, 153
Fonfría, J. P., Cernicharo, J., Richter, M. J., & Lacy, J. 2008, ApJ, 673, 445
Frisch, M. J., Trucks, G. W., Schlegel, H. B., et al. 2009, Gaussian 09, Revision D.01 (Wallingford, CT: Gaussian, Inc.)
Gottlieb, C. A., McCarthy, M. C., Travers, M. J., et al. 1998, J. Chem. Phys., 109, 5433
Gottlieb, C. A., McCarthy, M. C., & Thaddeus, P. 2010, ApJS, 189, 261
Gong, Y., Henkel, C., Spezzano, S., et al. 2015, A&A, 574, A56
Gordy, W., & Cook, R. 1984, Microwave Molecular Spectra, Techniques of Chemistry (New York: Wiley)
Guélin, M., Cernicharo, J., Navarro, S., et al. 1993, A&A, 182, L37
Hutchinson, M., Kroto, H. W., & Walton, D. R. M. 1980, J. Mol. Spectrosc., 82, 394
Iida, M., Ohshima, Y., & Endo, Y. 1991, ApJ, 371, L45
Kawaguchi, K., Kasai, Y., Ishikawa, S., & Kaifu, N. 1995, PASJ, 47, 853
Lee, C., Yang, W., & Parr, R. G. 1988, Phys. Rev. B, 37, 785
McCarthy, M. C., Levine, E. S., Apponi, A. J., & Thaddeus, P. 2000, J. Mol. Spectrosc., 203, 75
Møller, C., & Plesset, M. S. 1934, Phys. Rev., 46, 618
Müller, H. S. P., Schlöder, F., Stutzki, J., & Winnewisser, G. 2005, J. Mol. Struct., 742, 215
Pardo, J. R., & Cernicharo, J. 2007, ApJ, 654, 978
Pardo, J. R., Cernicharo, J., & Serabyn, E. 2001, IEEE Trans. Antennas Propag., 49, 12
Pardo, J. R., Cernicharo, J., Goicoechea, J. R., et al. 2004, ApJ, 615, L145
Pardo, J. R., Cernicharo, J., Goicoechea, J. R., et al. 2008, ApJ, 661, 250
Pardo, J. R., Cernicharo, J., Velilla-Prieto, L., et al. 2018, A&A, 615, L4
Patel, N. A., Young, K. H., Gottlieb, C. A., et al. 2011, ApJS, 193, 17
Pickett, H. M., Poynter, R. L., Cohen, E. A., et al. 1998, J. Quant. Spectrosc. Radiat. Transfer, 60, 883
Vichietti, R. M., & Haiduke, R. L. A. 2012, Spectrochim. Acta Part A, 90, 1
Wyrowski, F., Schilke, P., Thorwirth, S., et al. 2003, ApJ, 586, 344
Yamada, K. M. T., Degli Esposti, C., Botschwina, P., et al. 2004, A&A, 425, 767
Yamamoto, S., Saito, S., Guélin, M., et al. 1987, ApJ, 323, L149

Appendix A: Line frequencies

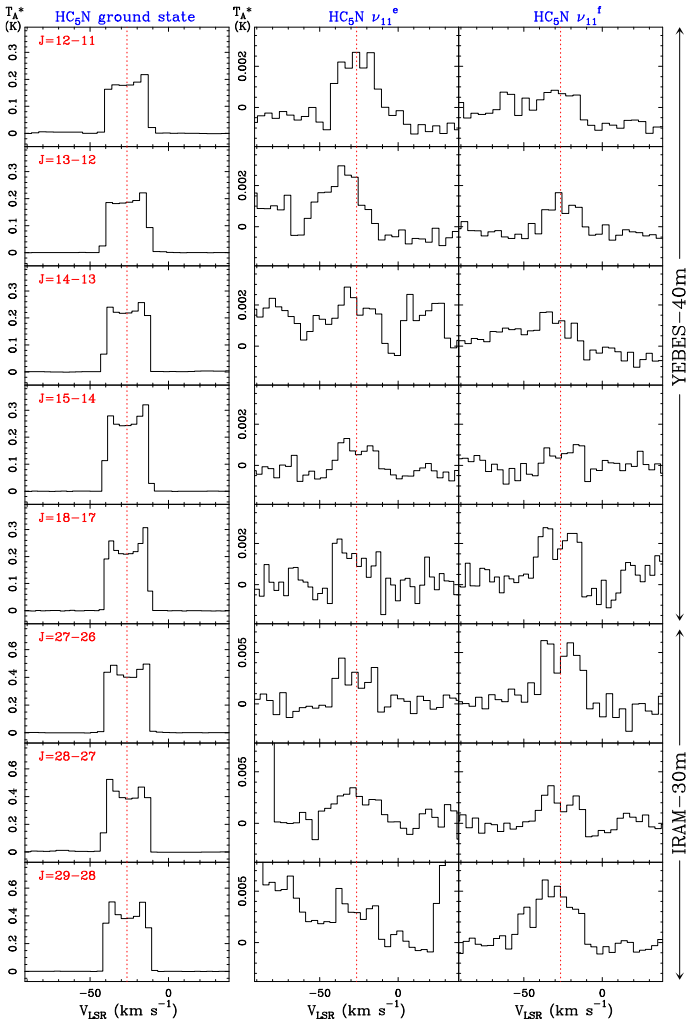

Fig. A.1. Observed lines of HC_5N with the Yebes 40 m and IRAM 30 m telescopes. The rotational quantum numbers are indicated in the top-right side of each panel. The same transitions for the ν_{11} state are shown in the middle (*e* component) and right panels (*f* component). The intensity scale is antenna temperature in mK. The abscissa corresponds to LSR velocities in km s^{-1}. The vertical red dotted line at −26.5 km s^{-1} indicates the systemic velocity of the envelope (Cernicharo et al. 2000, 2018).

The main goal of this paper is to study the emission from vibrationally excited states of the long cyanopolyynes HC_5N, HC_7N, and HC_9N. However, many lines in the 31–50 GHz and 70–116 GHz frequency ranges arise from the vibrationally excited states of the C_nH family of radicals. C_4H in its ν_7 and $2\nu_7$ states were previously reported in this source (Guélin et al. 1993), and its frequencies are well known from laboratory measurements (Yamamoto et al. 1987; Cooksy et al. 2015). C_6H in its ν_{11} state was detected and spectroscopically characterized in this source (Cernicharo et al. 2008). One of the doublets of this vibrational state of C_6H is shown in the top panel of Fig. 1. Additional laboratory information for this state was provided by Gottlieb et al. (2010). Most of these data have already been analyzed and further details will be published elsewhere (Pardo et al., in prep.). The following sections describe the data and the spectroscopic literature used in this work for HC_5N and HC_7N. We discussed HC_9N in Sect. 3, where observed lines are shown in Fig. 2 and

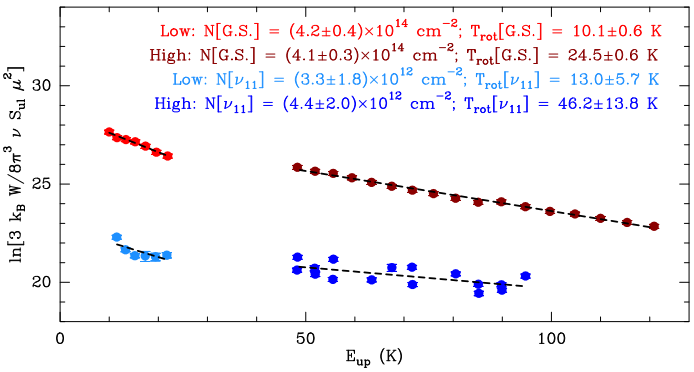

Fig. A.2. Rotational diagram for HC_5N in its ground state (red) and $\nu_{11} = 1$ vibrationally excited state (blue).

Table A.1. Vibrational partition function for $HC_{2n+1}N$ ($n = 2-5$).

Temperature (K)	HC_5N	HC_7N	HC_9N	$HC_{11}N$
10	1.00	1.00	1.00	1.04
15	1.00	1.01	1.02	1.15
20	1.00	1.03	1.07	1.34
25	1.00	1.08	1.16	1.60
30	1.01	1.14	1.27	1.93
35	1.02	1.22	1.41	2.35
40	1.04	1.32	1.57	2.87
45	1.06	1.43	1.78	3.50
50	1.09	1.56	2.01	4.28
60	1.17	1.87	2.61	6.39
80	1.38	2.74	4.49	14.07
100	1.69	4.09	7.83	30.51

observed frequencies are given in Table A.2. All these vibrationally excited states were implemented into the MADEX code (Cernicharo 2012), allowing for the calculation of column densities and the search for all their rotational lines in the 31–50 GHz and 70–116 GHz frequency ranges.

To evaluate the fraction of molecules in the different vibrational states for the typical temperatures of the external envelope (10–40 K) of IRC +10216, we calculated the vibrational partition function of these molecules using the standard expression (see, e.g. Gordy & Cook 1984)

$$Q_{\rm vib} = \prod_i (1 - e^{-(h\omega_i/KT)})^{-g_i}, \quad \text{(A.1)}$$

where ω_i and g_i represent the energy and the degeneracy of each vibrational mode i. For HC_9N, we used our ab initio values for the vibrational frequencies (see Appendix B). For HC_5N, HC_7N, and $HC_{11}N$, we used the calculations from Vichietti & Haiduke (2012). The results are given in Table A.1.

For low vibrational temperatures, the value of the vibrational partition function is dominated by the lowest energy vibrational state. In this case

$$Q_{\rm vib} = 1/(1 - e^{-(h\omega_l/KT_{\rm vib})})^{g_l}, \quad \text{(A.2)}$$

where ω_l and g_l are the frequency and the degeneracy of this lowest energy state and $T_{\rm vib}$ is the vibrational temperature. The abundance ratio between this level (we assume a bending mode, i.e. $g_l = 2$) and the ground state ($g = 1$) is given by N(v_l)/N(ground) $\simeq 2e^{-(h\omega_l/KT_{\rm vib})}$, where N(ground) is the column density in the

Table A.2. Observed line parameters of HC_9N.

HC_9N transition	ν_{rest} (MHz)	ν_{obs} (MHz)	$\int T_A^* dv$ (K km s^{-1})	v_{exp} (km s^{-1})	HC_9N transition	ν_{rest} (MHz)	ν_{obs} (MHz)	$\int T_A^* dv$ (K km s^{-1})	v_{exp} (km s^{-1})
J = 54–53	31375.437	31375.45(23)	0.245(01)	13.9(2.2)	v_{19}^e J = 68–67	39549.232	39549.22(05)	0.057(08)	14.1(0.4)
v_{19}^e J = 54–53	31407.067	31406.97(05)	0.064(01)	13.2(2.2)	v_{19}^f J = 68–67	39569.130	39569.11(05)	0.025(10)	14.5(0.1)
v_{19}^f J = 54–53	31422.868	31422.80(05)	0.039(13)	13.9(1.1)	J = 69–68	40090.398	40090.40(01)	0.118(01)	13.8(0.1)
J = 55–54	31956.443	31956.45(01)	0.199(12)	14.2(0.2)	v_{19}^e J = 69–68	40130.805	40130.83(05)	0.047(08)	16.1(0.4)
v_{19}^e J = 55–54	31988.658	31988.68(05)	0.037(01)	13.8(2.1)	v_{19}^f J = 69–68	40150.996	40151.01(05)	0.039(01)	13.7(0.2)
v_{19}^f J = 55–54	32004.752	32004.65(05)	0.074(12)	13.5(0.5)	J = 70–69	40671.385	40671.39(01)	0.123(01)	14.5(0.1)
J = 56–55	32537.448	32537.44(01)	0.156(01)	13.9(0.1)	v_{19}^e J = 70–69	40712.377	40712.34(05)	0.066(08)	14.5(0.1)
v_{19}^e J = 56–55	32570.248	32570.29(05)	0.072(01)	14.7(0.4)	v_{19}^f J = 70–69	40732.861	40732.80(05)	0.061(08)	14.3(0.3)
v_{19}^f J = 56–55	32586.635	32586.69(05)	0.084(01)	15.8(0.4)	J = 71–70	41252.370	41252.40(02)	0.112(07)	14.0(0.1)
J = 57–56	33118.451	33118.44(23)	0.173(01)	13.7(2.1)	v_{19}^e J = 71–70	41293.998	41294.00(05)	0.052(07)	17.7(0.5)
v_{19}^e J = 57–56	33151.837	33152.00(10)	0.081(12)	17.3(0.8)	v_{19}^f J = 71–70	41314.723	41314.71(05)	0.067(07)	17.5(0.5)
v_{19}^f J = 57–56	33168.516	33168.55(05)	0.058(01)	13.4(0.5)	J = 72–71	41833.354	41833.41(01)	0.130(01)	13.5(0.1)
J = 58–57	33699.454	33699.44(23)	0.179(01)	14.0(2.0)	v_{19}^e J = 72–71	41875.516	41876.57(05)	0.024(05)	14.5(0.0)
v_{19}^e J = 58–57	33733.425	33733.47(05)	0.078(01)	15.8(0.3)	v_{19}^f J = 72–71	41896.585	41896.52(05)	0.028(06)	14.5(0.1)
v_{19}^f J = 58–57	33750.397	33750.32(10)	.....*		J = 73–72	42414.336	42414.35(02)	0.099(01)	13.8(0.1)
J = 59–58	34280.455	34280.46(03)	0.183(01)	14.5(0.1)	v_{19}^e J = 73–72	42457.083	42457.14(10)	0.028(01)	13.4(0.5)
v_{19}^e J = 59–58	34315.011	34314.89(10)	.....*		v_{19}^f J = 73–72	42478.445	42478.45(05)	0.028(07)	13.3(0.4)
v_{19}^f J = 59–58	34332.275	34332.30(05)	0.065(01)	13.0(0.3)	J = 74–73	42995.317	42995.29(02)	0.137(07)	14.4(0.2)
J = 60–59	34861.455	34861.47(01)	0.157(01)	13.8(0.1)	v_{19}^e J = 74–73	43038.649	43038.60(10)	0.027(07)	13.2(0.3)
v_{19}^e J = 60–59	34896.594	34896.59(05)	0.052(01)	14.0(0.0)	v_{19}^f J = 74–73	43060.303	43060.35(15)	0.014(07)	14.5(0.0)
v_{19}^f J = 60–59	34914.154	34914.21(10)	0.094(01)	17.4(0.2)	J = 75–74	43576.297	43576.37(05)	0.093(07)	13.8(0.2)
J = 61–60	35442.454	35442.43(01)	0.172(01)	13.8(0.1)	v_{19}^e J = 75–74	43620.213	43620.23(10)	0.033(07)	15.7(1.4)
v_{19}^e J = 61–60	35478.180	35478.17(05)	0.050(01)	13.4(0.3)	v_{19}^f J = 75–74	43642.160	43642.25(10)	0.027(01)	13.3(0.3)
v_{19}^f J = 61–60	35496.031	35496.09(05)	0.060(01)	13.2(0.2)	J = 76–75	44157.275	44157.18(02)	0.072(07)	13.9(0.2)
J = 62–61	36023.452	36023.44(01)	0.166(01)	14.1(0.1)	v_{19}^e J = 76–75	44201.776	44201.78(07)	0.039(06)	17.5(1.4)
v_{19}^e J = 62–61	36059.763	36059.80(05)	0.059(01)	13.4(0.4)	v_{19}^f J = 76–75	44224.015	44224.14(10)	0.052(06)	16.0(0.5)
v_{19}^f J = 62–61	36077.906	36077.95(05)	0.088(10)	15.2(0.4)	J = 77–76	44738.251	44738.28(03)	0.051(06)	13.7(0.2)
J = 63–62	36604.448	36604.43(23)	0.151(01)	14.0(1.9)	v_{19}^e J = 77–76	44783.337	44783.23(10)	.....*	
v_{19}^e J = 63–62	36641.345	36641.44(05)	0.094(09)	21.5(1.5)	v_{19}^f J = 77–76	44805.869	44805.85(10)	.....*	
v_{19}^f J = 63–62	36659.780	36659.90(05)	0.047(09)	14.5(0.6)	J = 78–77	45319.225	45319.33(04)	0.093(06)	15.8(0.2)
J = 65–64	37766.437	37766.43(00)	0.160(01)	13.9(0.1)	v_{19}^e J = 78–77	45364.896	45364.41(10)	0.025(06)	12.9(0.5)
v_{19}^e J = 65–64	37804.504	37804.49(05)	0.044(01)	14.2(0.5)	v_{19}^f J = 78–77	45387.721	45387.43(10)	.....*	
v_{19}^f J = 65–64	37823.524	37823.51(05)	0.053(01)	13.4(0.2)	J = 79–78	45900.199	45900.08(05)	0.090(06)	14.2(0.2)
J = 66–65	38347.429	38347.46(03)	0.147(09)	14.2(0.2)	v_{19}^e J = 78–77	45946.454	45946.29(20)	.....*	
v_{19}^e J = 66–65	38386.081	38386.01(05)	0.034(01)	15.1(0.4)	v_{19}^f J = 78–77	45969.571	45969.41(10)	.....*	
v_{19}^f J = 66–65	38404.394	38404.98(30)	0.060(09)	15.1(0.8)	J = 80–79	46481.170	46481.30(03)	0.100(06)	14.6(0.3)
J = 67–66	38928.420	38928.42(02)	0.142(01)	13.8(0.1)	v_{19}^e J = 80–79	46528.010	46527.97(20)	.....*	
v_{19}^e J = 67–66	38967.657	38967.63(05)	0.050(01)	14.3(0.1)	v_{19}^f J = 80–79	46551.420	46551.65(20)	0.082(06)	13.7(0.3)
v_{19}^f J = 67–66	38987.263	38987.24(05)	0.017(01)	13.9(0.7)	J = 82–81	47643.108	47643.13(05)	0.050(06)	13.0(0.3)
J = 68–67	39509.410	39509.40(01)	0.146(01)	13.9(0.1)	J = 83–82	48224.074	48224.14(05)	0.038(05)	13.7(0.4)

Notes. Numbers in parentheses represent the derived uncertainty (1σ) of the parameter in units of the last digit. This molecular species is only visible in the Yebes 40 m telescope data. (*)The line is partially blended with another feature but a fit to the frequency can be obtained by fixing the expanding velocity to 14.5 km s^{-1}. However, the integrated line intensity is very uncertain and it is not used for the rotational diagrams.

ground state, N(ground) = N_T/Q_{vib}, and N_T is the total number of molecules in all vibrational states.

For a vibrational temperature of 20 K, and using the frequencies in Table B.4, we obtain

N(HC_5N ν_{11})/N(HC_5N ground state) ≃ 0.00,
N(HC_7N ν_{15})/N(HC_7N ground state) ≃ 0.04,
N(HC_9N ν_{19})/N(HC_9N ground state) ≃ 0.05,

while for a vibrational temperature of 50 K we obtain

N(HC_5N ν_{11})/N(HC_5N ground state) ≃ 0.08,
N(HC_7N ν_{15})/N(HC_7N ground state) ≃ 0.41,
N(HC_9N ν_{19})/N(HC_9N ground state) ≃ 0.46,

that is to say, for a vibrational temperature of 50 K, HC_7N and HC_9N will have a significant fraction of molecules in their lowest energy bending modes (ν_{15} and ν_{19}). However, HC_5N would need higher vibrational temperatures to have a significant fraction of molecules in its ν_{11} mode.

A.1. HC_5N

For HC_5N, the rotational spectrum was measured in the laboratory for several vibrationally excited states involving the ν_6, ν_7, ν_8, ν_9, ν_{10}, and ν_{11} modes, including fundamental bands, overtones, and combination bands (Hutchinson et al. 1980; Yamada et al. 2004; Degli Esposti et al. 2005). In this

Table A.3. Same as Table A.2 but for HC_7N.

HC_7N transition	ν_{rest} (MHz)	ν_{obs} (MHz)	$\int T_A^* dv$ (K km s^{-1})	v_{exp} (km s^{-1})	HC_7N transition	ν_{rest} (MHz)	ν_{obs} (MHz)	$\int T_A^* dv$ (K km s^{-1})	v_{exp} (km s^{-1})
$J = 28–27$	31583.709	31583.69(01)	1.627(13)	13.9(0.1)	$J = 41–40$	46246.979	46247.14(01)	1.494(12)	14.9(0.1)
v_{15}^e $J = 28–27$	31623.211	31623.93(06)	0.190(13)	19.3(0.6)	v_{15}^e $J = 41–40$	46304.799	46304.64(07)	0.089(06)	15.3(0.4)
v_{15}^e $J = 28–27$	31643.340	31643.18(03)	0.038(13)	13.6(1.3)	v_{15}^f $J = 41–40$	46334.246	46334.27(01)	0.035(06)	13.5(0.1)
$J = 29–28$	32711.672	32711.65(01)	1.588(01)	13.8(0.1)	$J = 42–41$	47374.898	47374.84(01)	0.836(06)	13.8(0.1)
v_{15}^e $J = 29–28$	32752.583	32752.58(23)	0.095(01)	13.7(2.1)	v_{15}^f $J = 42–41$	47464.288	47464.24(01)	0.079(06)	13.7(0.2)
v_{15}^f $J = 29–28$	32773.430	32773.42(23)	0.083(01)	13.9(2.1)	$J = 43–42$	48502.813	48502.78(01)	0.862(22)	13.7(0.1)
$J = 30–29$	33839.632	33839.61(01)	1.595(11)	13.7(0.1)	v_{15}^e $J = 43–42$	48563.449	48563.49(02)	0.081(05)	14.1(0.3)
v_{15}^e $J = 30–29$	33881.953	33881.85(07)	0.110(01)	14.5(0.2)	v_{15}^f $J = 43–42$	48594.326	48593.61(23)	0.107(05)	29.9(1.4)
v_{15}^f $J = 30–29$	33903.518	33903.52(05)	0.088(01)	14.1(0.2)	$J = 44–43$	49630.723	49630.68(01)	0.680(10)	13.9(0.1)
$J = 31–30$	34967.589	34967.59(01)	1.525(10)	14.1(0.1)	$J = 63–62$	71060.102	71060.14(03)	0.546(09)	14.0(0.1)
v_{15}^e $J = 31–30$	35011.320	35011.24(04)	0.103(10)	13.1(0.4)	v_{15}^f $J = 63–62$	71193.996	71193.72(29)	0.110(13)	17.4(0.9)
v_{15}^f $J = 31–30$	35033.602	35033.62(04)	0.093(10)	13.7(0.3)	$J = 64–63$	72187.909	72187.92(02)	0.517(08)	13.0(0.1)
$J = 32–31$	36095.543	36095.49(01)	1.479(19)	13.5(0.1)	v_{15}^e $J = 64–63$	72278.073	72279.00(26)	0.046(08)	12.0(0.9)
v_{15}^e $J = 32–31$	36140.683	36140.68(01)	0.126(01)	14.0(0.2)	$J = 65–64$	73315.709	73315.82(02)	0.482(04)	13.3(0.1)
v_{15}^f $J = 32–31$	36163.683	36163.72(04)	0.126(01)	14.1(0.2)	v_{15}^f $J = 65–64$	73453.831	73453.68(23)	0.073(12)	14.7(0.8)
$J = 33–32$	37223.494	37223.49(01)	1.611(09)	13.9(0.1)	$J = 66–65$	74443.504	74443.58(03)	0.419(08)	13.5(0.1)
v_{15}^e $J = 33–32$	37270.044	37270.03(53)	0.100(46)	13.7(2.5)	v_{15}^e $J = 66–65$	74536.476	74536.36(99)	0.032(12)	13.9(0.9)
v_{15}^f $J = 33–32$	37293.760	37293.59(03)	0.091(09)	13.7(0.2)	$J = 67–66$	75571.292	75571.33(03)	0.402(08)	13.5(0.1)
$J = 34–33$	38351.442	38351.42(01)	1.448(01)	14.1(0.1)	v_{15}^f $J = 67–66$	75713.639	75713.25(21)	0.083(16)	13.6(0.9)
v_{15}^e $J = 34–33$	38399.401	38399.49(04)	0.086(09)	14.4(0.3)	$J = 68–67$	76699.073	76698.89(05)	0.417(12)	14.5(0.2)
v_{15}^f $J = 34–33$	38423.834	38423.77(02)	0.112(09)	14.4(0.2)	v_{15}^f $J = 68–67$	76843.532	76839.11(05)	0.059(08)	12.3(0.2)
$J = 35–34$	39479.387	39479.37(01)	1.489(08)	13.9(0.1)	$J = 69–68$	77826.848	77826.95(99)	0.404(04)	14.9(0.9)
v_{15}^e $J = 35–34$	39528.755	39528.72(23)	0.081(01)	13.2(1.7)	v_{15}^e $J = 69–68$	77924.029	77923.56(20)	0.061(08)	13.8(0.9)
v_{15}^f $J = 35–34$	39553.904	39553.77(03)	0.081(01)	13.9(0.2)	$J = 70–69$	78954.616	78954.86(11)	0.350(23)	13.8(0.4)
$J = 36–35$	40607.328	40607.31(01)	1.377(08)	13.8(0.1)	v_{15}^f $J = 70–69$	79103.297	79103.76(19)	0.053(11)	12.1(0.9)
v_{15}^e $J = 36–35$	40658.105	40658.13(02)	0.092(08)	13.5(0.2)	$J = 71–70$	80082.377	80082.05(39)	0.455(86)	15.0(0.9)
v_{15}^f $J = 36–35$	40683.971	40683.94(04)	0.092(01)	14.0(0.2)	$J = 73–72$	82337.879	82340.09(02)	1.128(18)	14.3(0.1)
$J = 37–36$	41735.265	41735.28(01)	1.340(07)	14.3(0.1)	$J = 74–73$	83465.620	83465.80(12)	0.133(14)	13.6(0.4)
v_{15}^e $J = 37–36$	41787.451	41787.41(03)	0.080(07)	13.9(0.3)	$J = 75–74$	84593.353	84593.21(04)	0.194(07)	13.9(0.1)
v_{15}^f $J = 37–36$	41814.034	41814.03(03)	0.109(07)	14.7(0.2)	$J = 76–75$	85721.079	85721.09(04)	0.175(03)	13.6(0.1)
$J = 38–37$	42863.199	42863.16(01)	1.201(07)	13.8(0.1)	$J = 78–77$	87976.509	87976.32(08)	0.147(07)	15.4(0.2)
v_{15}^e $J = 38–37$	42916.794	42916.86(03)	0.110(07)	13.6(0.2)	$J = 80–79$	90231.908	90231.94(06)	0.113(03)	14.6(0.2)
$J = 39–38$	43991.130	43991.15(01)	1.101(07)	14.0(0.1)	$J = 81–80$	91359.596	91359.49(15)	0.072(07)	13.4(0.5)
v_{15}^e $J = 39–38$	44046.133	44046.17(04)	0.072(07)	13.8(0.3)	$J = 85–84$	95870.270	95870.39(17)	0.088(09)	14.7(0.4)
v_{15}^f $J = 39–38$	44074.148	44074.21(03)	0.098(07)	14.6(0.2)	$J = 86–85$	96997.918	96996.26(19)	0.068(06)	17.6(0.4)
$J = 40–39$	45119.056	45119.07(01)	0.928(06)	14.1(0.1)	$J = 87–86$	98125.557	98124.86(22)	0.098(09)	16.4(0.6)
v_{15}^f $J = 40–39$	45204.199	45204.11(04)	0.074(06)	13.8(0.2)	$J = 88–87$	99253.189	99251.05(12)	0.118(06)	16.4(0.4)
					$J = 89–88$	100380.811	100381.25(68)	0.021(09)	13.3(0.9)

Notes. Observations below 50 GHz are with the Yebes 40 m telescope, all others are with the IRAM 30 m.

work, we detected the lowest energy state ν_{11}. Table A.4 provides the line parameters for all lines of HC_5N in its ground and ν_{11} states observed in the 31–50 GHz and 70–116 GHz ranges. Figure A.1 shows some of the observed lines of HC_5N in these states. We have searched without success for lines arising from the $\nu_{11} = 2$, $\nu_{10} = 1$, and $\nu_{10} + \nu_{11}$ vibrational states within the observed frequency domains. These states lie at energies of ≈222, 264, and 374 cm^{-1}, respectively, above the ground state (Vichietti & Haiduke 2012).

From the observed intensities of HC_5N and its ν_{11} state, we performed a rotational diagram analysis. The results are shown in Fig. A.2. For the ground state, two different slopes, corresponding to two different rotational temperatures, were found. For low-J transitions in the Q-band, we derived $T_{rot} = 10.1 \pm 0.6$ K and $N(HC_5N) = 4.2 \pm 0.4 \times 10^{14}$ cm^{-2}. The high-J data at 3 mm indicate a higher rotational temperature of 24.5 ± 0.6 K and a column density of $4.1 \pm 0.3 \times 10^{14}$ cm^{-2}. The lines of the ν_{11} state are detected in the Q-band and the 3 mm domain and also show two different regimes: a low temperature component $T_{rot} = 13.0 \pm 5.7$ K and $N(HC_5N\ \nu_{11}) = 3.3 \pm 1.8 \times 10^{12}$ cm^{-2}; and a high temperature component with $T_{rot} = 46.2 \pm 13.8$ K and $N(HC_5N\ \nu_{11}) = 4.4 \pm 2.0 \times 10^{12}$ cm^{-2}. The observed column density ratio between the ground and the ν_{11} states is 127 ± 60 and 93 ± 50 for the cold and warm components, respectively. Consequently, the correction to the total column density of HC_5N due to its vibrational state ν_{11} is ≃1%, that is to say the ground state contains more than 99% of the molecules. The observed column density ratio suggests a vibrational temperature ≃30 K, similar to the rotational temperature of the warm component.

A.2. HC_7N

The rotational spectrum of HC_7N in vibrationally excited states was recorded in the laboratory for ν_{13}, ν_{14}, and $\nu_{15} = 1, 2, 3$ (Bizzocchi & Degli 2004). In this work, we detected all the lines of the $\nu_{15} = 1$ state and some of the $\nu_{15} = 2$ state within the covered 31–50 GHz frequency range. These two states lie at energies of ≈62 and 124 cm^{-1}, respectively, above the ground state

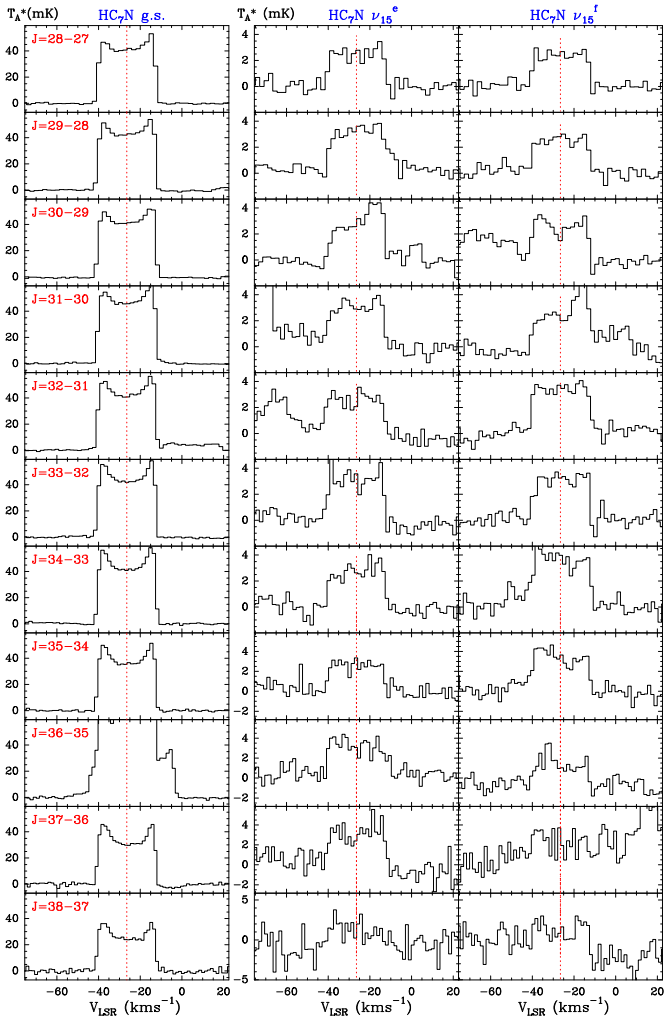

Fig. A.3. Observed lines of HC_7N with the Yebes 40 m telescope. The rotational quantum numbers are indicated in the top-left side of each panel. The same transitions for the v_{15} state are shown in the middle (e component) and right panels (f component). The intensity scale is antenna temperature in mK. The abscissa corresponds to LSR velocities in km s^{-1}. The vertical red dotted line at −26.5 km s^{-1} indicates the systemic velocity of the envelope (Cernicharo et al. 2000, 2018).

(Botschwina et al. 1997; Vichietti & Haiduke 2012). In the 70–116 GHz frequency range, only a few lines of the v_{15} state are detected. Table A.3 gives the line parameters for the observed transitions of HC_7N in its ground and vibrationally excited states, $v_{15} = 1$ and $v_{15} = 2$. Figure A.3 shows a selected sample of the observed lines. We have searched without success for lines arising from the v_{14}, and v_{13} vibrational states within the covered frequency ranges. These states lie at energies of ≈163 and 280 cm^{-1}, respectively, above the ground state (Botschwina et al. 1997; Vichietti & Haiduke 2012).

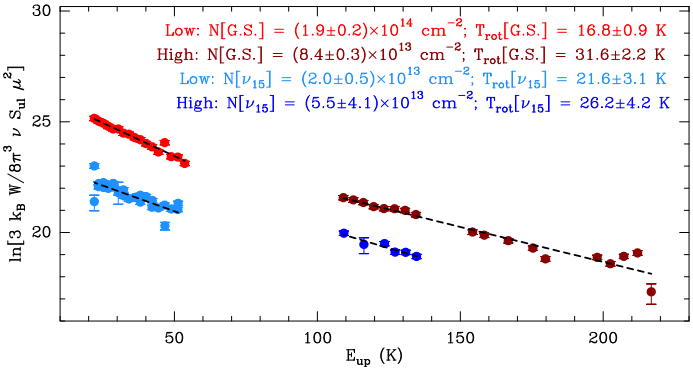

Fig. A.4. Rotational diagram for HC_7N in its ground state (red) and $v_{15} = 1$ vibrationally excited state (blue).

From the observed intensities of HC_7N and its v_{15} state, we performed a rotational diagram analysis. The results are shown in Fig. A.4. For the ground state, two different slopes, corresponding to two different rotational temperatures, were found; that is to say, the molecule shows a similar behavior to that of HC_5N. For low-J transitions in the Q-band, we derived $T_{rot} = 16.8 \pm 0.9$ K and N(HC_7N) = $1.9 \pm 0.2 \times 10^{14}$ cm^{-2}. The high-J data at 3 mm indicate a higher rotational temperature of 32.6 ± 2.2 K and a column density of $8.4 \pm 0.3 \times 10^{13}$ cm^{-2}. The lines of the v_{15} state are mainly detected in the Q-band, for which we derive $T_{rot} = 21.6 \pm 3.1$ K and N(HC_7N v_{15}) = $2.0 \pm 0.5 \times 10^{13}$ cm^{-2}. Only a few rotational lines within the v_{15} vibrational state were detected in the 3 mm domain and they are too weak to derive a reasonable rotational temperature and column density. For the Q-band data, which cover lines from $J_{up} = 28$ up to $J_{up} = 44$, the observed column density ratio between the ground and v_{15} states is 9.5 ± 3.4. Consequently, the correction to the total column density of HC_7N due to its vibrational state v_{15} is ≃10%. Although the effect in the total column density is negligible, the observed column density in the v_{15} level is a factor of ∼3 higher that the one we would expect if the vibrational levels were under thermodynamic equilibrium at the derived T_{rot}. The observed column density ratio suggests a vibrational temperature of ≃30 K. As discussed in this letter, the increase in the population of the v_{15} level is due to IR pumping from the ground state by absorption of IR photons coming from the central source and the subsequent IR radiative decay cascades. From the observed intensities of the $v_{15} = 2$ lines, we derive a column density ratio of N($v_{15} = 1$)/N($v_{15} = 2$) ≃ 5, which is also compatible with a vibrational temperature of 30 K. It is worth noting that this vibrational temperature is similar to the rotational temperature of the high-J lines of HC_7N observed in the 3 mm domain, 26.2 ± 4.2 K. The effect of IR pumping on the ground state is, hence, to pump molecules from low-J levels to high-J ones.

Table A.4. Same as Table A.2 but for HC_5N.

HC_5N transition	ν_{rest} (MHz)	ν_{obs} (MHz)	$\int T_A^* dv$ (K km s^{-1})	v_{exp} (km s^{-1})	HC_5N transition	ν_{rest} (MHz)	ν_{obs} (MHz)	$\int T_A^* dv$ (K km s^{-1})	v_{exp} (km s^{-1})
J = 12–11	31951.776	31951.75(01)	6.993(01)	13.8(0.1)	J = 30–29	79876.710	79876.74(01)	11.251(15)	14.2(0.1)
J = 13–12	34614.385	34614.34(01)	6.615(21)	13.8(0.1)	J = 31–30	82539.039	82539.01(01)	9.795(14)	14.0(0.1)
v_{11}^f J = 13–12	34701.825	34701.76(04)	0.042(01)	13.9(0.5)	v_{11}^f J = 31–30	82747.345	82747.57(28)	0.069(04)	15.5(0.2)
J = 14–13	37276.985	37276.92(01)	7.374(46)	13.7(0.1)	J = 32–31	85201.346	85201.29(01)	8.809(35)	14.0(0.1)
v_{11}^e J = 14–13	37371.147	37371.42(02)	0.027(01)	12.6(0.1)	v_{11}^f J = 32–31	85416.355	85416.69(28)	0.141(25)	14.5(0.9)
J = 15–14	39939.574	39939.55(01)	7.910(01)	14.1(0.0)	J = 33–32	87863.630	87863.64(01)	7.872(15)	14.2(0.1)
v_{11}^e J = 15–14	40005.587	40006.27(40)	0.008(01)	9.3(0.5)	v_{11}^e J = 33–32	88008.742	88008.76(05)	0.157(03)	14.5(0.2)
v_{11}^f J = 15–14	40040.459	40040.28(06)	0.024(01)	12.5(0.5)	v_{11}^f J = 33–32	88085.340	88085.56(09)	0.065(03)	14.3(0.3)
J = 16–15	42602.153	42602.15(01)	7.448(14)	13.9(0.1)	J = 34–33	90525.889	90525.86(01)	7.195(01)	14.1(0.1)
v_{11}^e J = 16–15	42672.564	42672.84(02)	0.118(07)	13.0(0.2)	J = 35–34	93188.125	93188.09(01)	6.170(01)	14.1(0.1)
v_{11}^f J = 16–15	42709.759	42709.81(10)	0.028(07)	14.2(0.8)	v_{11}^e J = 35–34	93342.013	93343.95(09)	0.132(06)	20.2(0.7)
J = 17–16	45264.720	45264.71(01)	6.313(19)	13.9(0.1)	J = 36–35	95850.335	95850.45(01)	5.428(01)	14.4(0.1)
v_{11}^e J = 17–16	45339.530	45339.31(10)	0.031(06)	11.9(0.7)	v_{11}^e J = 36–35	96008.609	96008.60(09)	0.084(06)	14.0(0.6)
J = 18–17	47927.274	47927.24(01)	5.907(06)	14.0(0.1)	v_{11}^f J = 36–35	96092.138	96093.26(02)	0.053(06)	16.6(0.1)
v_{11}^f J = 18–17	48048.321	48048.39(05)	0.038(05)	12.1(0.3)	J = 37–36	98512.519	98512.53(99)	5.984(06)	14.1(0.9)
J = 27–26	71889.595	71889.55(01)	13.971(36)	14.0(0.1)	v_{11}^e J = 37–36	98675.179	98676.00(09)	0.088(06)	13.5(0.9)
v_{11}^e J = 27–26	72008.362	72008.55(04)	0.075(01)	13.2(0.4)	v_{11}^f J = 37–36	98761.017	98761.06(10)	0.067(06)	13.6(0.3)
v_{11}^f J = 27–26	72071.074	72070.92(13)	0.145(12)	12.9(0.5)	J = 38–37	101174.676	101174.67(01)	5.017(09)	14.0(0.1)
J = 28–27	74551.987	74551.96(01)	12.753(99)	14.0(0.1)	v_{11}^e J = 38–37	101341.721	101345.95(09)	0.148(15)	14.6(0.4)
v_{11}^e J = 28–27	74675.147	74675.72(09)	0.092(12)	20.6(9.9)	J = 39–38	103836.806	103836.81(01)	4.230(35)	14.1(0.1)
v_{11}^f J = 28–27	74740.175	74740.16(17)	0.068(08)	13.1(0.5)	J = 40–39	106498.908	106498.90(01)	3.962(08)	13.9(0.1)
J = 29–28	77214.359	77214.32(01)	12.709(12)	14.0(0.1)	J = 41–40	109160.981	109161.23(01)	3.380(05)	14.7(0.1)
v_{11}^e J = 29–28	77341.911	77341.90(09)	0.058(04)	13.2(0.4)	J = 42–41	111823.024	111823.04(01)	2.916(19)	13.8(0.1)
v_{11}^f J = 29–28	77409.254	77410.89(16)	0.162(08)	21.7(0.8)	J = 43–42	114485.037	114485.12(02)	2.549(34)	13.7(0.1)

Notes. Observations below 50 GHz are with the Yebes 40 m telescope, all others are with the IRAM 30 m.

Appendix B: Quantum chemical calculations for HC_9N vibrationally excited states

We carried out quantum chemical calculations to obtain accurate values of the spectroscopic parameters necessary to assign the new spectral features. These parameters are the rotational constant B and the l-type doubling constant q^e. To obtain these parameters for the vibrationally excited states of HC_9N, we performed anharmonic frequency calculations. We used two different levels of theory for this purpose: density functional theory (DFT) calculations with the B3LYP functional (Lee et al. 1988) and the Møller–Plesset post-Hartree–Fock method (Møller & Plesset 1934), using explicitly electron correlation effects through perturbation theory up to second order (MP2). The Dunning basis set with consistent polarized valence triple-ζ (cc-pVTZ) was used in both calculation methods. The use of coupled cluster methods was not considered because of their large computing time. All the calculations were performed using the Gaussian 09 program package (Frisch et al. 2009). A previous theoretical study on the vibrationally excited states of HC_9N, including other cyanopolyynes, was published by Vichietti & Haiduke (2012). However, the authors only provide the vibrational band frequencies and intensities under the harmonic approximation. The results of our anharmonic calculations in terms of energy and intensities are compatible with those reported by Vichietti & Haiduke (2012).

The value of B_v for each vibrationally excited state of HC_9N can be determined using the values of the first order vibration-rotation coupling constants α_i, which are different for each vibrational state and are obtained from the anharmonic frequency calculations. Values of B_v can be derived using the expression (Gordy & Cook 1984)

$$B_v = B_e - \sum_i \alpha_i \left(v_i + \tfrac{1}{2} d_i\right), \tag{B.1}$$

where B_v and B_e are the rotational constant in a given excited state and in equilibrium, respectively, v_i is the vibrational quantum number, and d_i is the corresponding degeneracy of the state. On the other hand, the values for the l-type doubling constant q_v^e can be directly obtained from the frequency calculations.

Table B.1 shows the vibration-rotation coupling constants α_i and the l-type doubling constant q_i^e for each vibrationally excited state i of HC_9N obtained from the B3LYP and MP2 calculations. The estimated rotational constants for each vibrationally excited state were calculated as described above using the B_{ground} constant for the ground state determined by Iida et al. (1991). The anharmonic vibrational frequencies and the IR intensities of the corresponding fundamental bands are also shown in Table B.1. The assignment of the observed transitions to the vibrationally excited state $v_{19} = 1$ is based on the excellent agreement between the experimental and predicted values for B_{19} and the $q_{v_{19}}^e$. It can be observed that the accordance between the experimental and predicted values is a bit better when the B3LYP/cc-pVTZ level of theory is used. However, the theoretical results for both methods indicate that the assignment is unequivocal regardless of the level of the calculation. Further evidence in support of this assignment is related to the vibrational frequency. Using the experimental values derived from the rotational analysis and the approximate expression $\omega_v \approx 2.6 B_v^2/q_{vt}$ (Gordy & Cook 1984), the obtained value for the vibrational frequency is only compatible with the assignment of the series of lines to the v_{19} state.

The reliability of both methods of calculation used for HC_9N was first tested for the analogue molecular systems

Table B.1. Theoretical values for the vibrational excited states of HC_9N calculated at B3LYP/cc-pVTZ and MP2/cc-pVTZ levels of theory under the anharmonic approach.

		α_i (MHz)		B_v (MHz) [a]		q_v^e (MHz)		Frequency (cm^{-1})	
Vib. State	Sim.	B3LYP	MP2	B3LYP	B3LYP	B3LYP	MP2	B3LYP	MP2
ν_1	σ	0.07761	0.07485	290.44071	290.44347	–	–	3336	3348
ν_2	σ	0.40988	0.52794	290.10844	289.99038	–	–	2296	2142
ν_3	σ	0.48562	0.47154	290.03270	290.04678	–	–	2253	2090
ν_4	σ	0.62642	0.60274	289.89190	289.91558	–	–	2182	2023
ν_5	σ	0.34994	0.33200	290.16838	290.18632	–	–	2173	2028
ν_6	σ	0.29256	0.33625	290.22576	290.18207	–	–	2088	1956
ν_7	σ	0.50556	0.47858	290.01276	290.03974	–	–	1406	1383
ν_8	σ	0.31723	0.30450	290.20109	290.21382	–	–	1128	1098
ν_9	σ	0.19501	0.18891	290.32331	290.32941	–	–	737	744
ν_{10}	σ	0.08457	0.08156	290.43375	290.43676	–	–	377	365
ν_{11}	π	–0.03612	–0.03210	290.55444	290.55042	0.0101	0.0103	653	601
ν_{12}	π	–0.22177	–0.25210	290.74009	290.77042	0.0128	0.0134	545	459
ν_{13}	π	–0.18431	–0.20526	290.70263	290.72358	0.0138	0.0139	535	491
ν_{14}	π	–0.19463	–0.19918	290.71295	290.71750	0.0143	0.0145	510	477
ν_{15}	π	–0.21125	–0.22289	290.72957	290.74121	0.0161	0.0160	450	430
ν_{16}	π	–0.27911	–0.28303	290.79743	290.80135	0.0205	0.0208	309	285
ν_{17}	π	–0.27102	–0.26584	290.78934	290.78416	0.0300	0.0298	208	198
ν_{18}	π	–0.29291	–0.28753	290.81123	290.80585	0.0537	0.0530	122	110
ν_{19}	π	–0.35317	–0.34513	290.87149	290.86345	0.1408	0.1378	55	47
Exp. (ν_{19}) [b]				290.884436 (345)		0.146310(133)		50 [d]	
Error [c]				0.004%	0.007%	3.8%	5.8%	10.0%	6.0%

Notes. [a]Rotational constant B of the vibrational state ν calculated using the experimental value of the ground state from Iida et al. (1991). [b]Experimental values obtained form a fit to the frequencies observed in this work (see Table A.2). [c]Discrepancies between theoretical calculations and experimental values for the vibrational excited state ν_{19}. Values calculated as follows: ((Exp – Theo) / Exp) × 100. [d]Calculated using the approximation $\omega_v \approx 2.6 B_v^2/q_{vt}$, where ω_v is the frequency of the vibrational state ν and B_v and q_{vt} are its rotational and l-doubling constants, respectively.

Table B.2. Comparison between experimental and theoretical values, using the anharmonic approximation at B3LYP/cc-pVTZ level of theory, for the vibrationally excited states of HC_5N and HC_7N.

Vib. State	Theo. B_v [a] (MHz)	Exp. B_v [b] (MHz)	B_v [c] %Error	Theo. q_v^e [d] (MHz)	Exp. q_v^e [e] (MHz)	q_v^e [c] %Error
HC_5N						
ν_6	1330.2385	1330.27109(88) [f]	0.002%	–	–	–
ν_7	1331.6481	1331.600997(28) [f]	–0.004%	0.2041	0.213887(55) [f]	4.6%
ν_8	1333.2083	1333.051138(27) [f]	–0.012%	0.3102	0.316154(59) [f]	1.9%
ν_9	1332.8278	1332.925330(20) [g]	0.007%	0.3120	0.328526(40) [g]	5.0%
ν_{10}	1333.6142	1333.784785(26) [g]	0.013%	0.4645	0.500190(52) [g]	7.1%
ν_{11}	1333.9370	1334.118237(24) [g]	0.014%	1.1066	1.162898(48) [g]	4.8%
HC_7N						
ν_{13}	564.696253	564.736752(39) [h]	0.007%	0.0793	0.085553(77) [h]	7.3%
ν_{14}	564.711383	564.743284(47) [h]	0.006%	0.1358	0.143602(94) [h]	5.4%
ν_{15}	564.855313	564.887305(34) [h]	0.006%	0.3444	0.359762(69) [h]	4.3%

Notes. [a]Rotational constant B of the vibrational state ν estimated using the theoretical vibration–rotation coupling constants α_i calculated at the B3LYP/cc-pVTZ level of theory. [b]Experimental values of the B rotational constant. [c]Discrepancies between theoretical calculations and experimental values calculated as follows: ((Exp – Theo) / Exp) × 100. [d]l-doubling constant q_v^e of the vibrational mode ν calculated at the B3LYP/cc-pVTZ level of theory. [e]Experimental value of the l-doubling constant q_{vt}. [f]Experimental values are taken from Degli Esposti et al. (2005). [g]Experimental values are taken from Yamada et al. (2004). [h]Experimental values are taken from Bizzocchi & Degli (2004).

HC_5N and HC_7N to rule out any kind of doubt in the assignment. Tables B.2 and B.3 show the results of anharmonic calculations for HC_5N and HC_7N at both B3LYP/cc-pVTZ and MP2/cc-pVTZ levels of theory. The values of B_v and q_v^e calculated for HC_5N and HC_7N are compared to those reported experimentally (Bizzocchi & Degli 2004; Yamada et al. 2004; Degli Esposti et al. 2005). We see that the predicted values with both levels of theory reproduce the experimental values for the two molecules very well. The errors obtained for HC_5N and HC_7N are on the same order of those found for the ν_{19} mode

Table B.3. Comparison between experimental and theoretical values, using the anharmonic approximation at MP2/cc-pVTZ level of theory, for the vibrationally excited states of HC_5N and HC_7N.

Vib. State HC_5N	Theo. B_v [a]	Exp. B_v [b]	B_v [c]	Theo. q_v^e [d]	Exp. q_v^e [e]	q_v^e [c]
ν_6	1330.229	1330.27109(88) [f]	0.003%	–	–	–
ν_7	1331.651	1331.600997(28) [f]	–0.004%	0.2017	0.213887(55) [f]	–5.7%
ν_8	1333.224	1333.051138(27) [f]	–0.013%	0.2986	0.316154(59) [f]	–5.6%
ν_9	1332.841	1332.925330(20) [g]	0.006%	0.3094	0.328526(40) [g]	–5.8%
ν_{10}	1333.634	1333.784785(26) [g]	0.011%	0.4651	0.500190(52) [g]	–7.0%
ν_{11}	1333.959	1334.118237(24) [g]	0.012%	1.0892	1.162898(48) [g]	–6.3%
HC_7N						
ν_{13}	564.713	564.736752(39) [h]	0.004%	0.0809	0.085553(77) [h]	–5.5%
ν_{14}	564.705	564.743284(47) [h]	0.007%	0.1350	0.143602(94) [h]	–6.0%
ν_{15}	564.845	564.887305(34) [h]	0.007%	0.3392	0.359762(69) [h]	–5.7%

Notes. [a]Rotational constant B of the vibrational state v estimated using the theoretical vibration–rotation coupling constants α_i calculated at the MP2/cc-pVTZ level of theory. [b]Experimental values of the B rotational constant. [c]Discrepancies between theoretical calculations and experimental values calculated as follows: ((Exp – Theo) / Exp) × 100. [d]l-doubling constant q_v^e of the vibrational mode v calculated at the MP2/cc-pVTZ level of theory. [e]Experimental value of the l-doubling constant q_{vt}. [f]Experimental values are taken from Degli Esposti et al. (2005). [g]Experimental value are taken from Yamada et al. (2004). [h]Experimental values are taken from Bizzocchi & Degli (2004).

Table B.4. Calculated energies and IR intensities of the fundamental bands of all the vibrational modes of HC_5N, HC_7N, and HC_9N.

	HC_9N				HC_7N				HC_5N			
	Energy [a]		Intensity [b]		Energy		Intensity		Energy		Intensity	
State	MP2 [c]	B3LYP [c]	MP2	B3LYP	MP2	B3LYP	MP2	B3LYP	MP2	B3LYP	MP2	B3LYP
ν_1	3348	3336	131.766	175.048	3349	3330	113.779	145.945	3350	3327	101.387	107.211
ν_2	2142	2296	5.710	98.808	2139	2311	3.561	61.568	2167	2308	32.819	77.124
ν_3	2090	2253	0.671	0.138	2104	2223	84.796	114.308	2102	2246	4.246	6.556
ν_4	2023	2182	171.359	275.899	2054	2192	3.509	4.467	1981	2116	0.024	0.509
ν_5	2028	2173	28.766	51.419	1969	2097	1.918	0.060	1174	1201	0.036	0.443
ν_6	1956	2088	2.473	0.791	1305	1322	1.674	0.200	611	632	0.325	0.026
ν_7	1383	1406	0.004	0.748	881	911	0.071	1.800	611	644	39.608	41.287
ν_8	1098	1128	0.693	0.241	458	470	0.407	0.110	461	546	0.829	2.414
ν_9	744	737	0.855	3.752	607	640	37.719	42.675	463	494	0.438	0.101
ν_{10}	365	377	0.531	0.230	455	539	0.602	1.765	252	271	5.677	8.631
ν_{11}	601	653	39.013	43.229	487	522	1.667	0.667	109	113	0.202	0.376
ν_{12}	459	545	0.061	1.956	441	461	1.066	2.715				
ν_{13}	491	535	2.770	0.821	273	290	0.098	0.007				
ν_{14}	477	510	0.329	3.882	160	162	5.288	5.713				
ν_{15}	430	450	0.346	0.005	58	52	0.111	0.039				
ν_{16}	285	309	2.950	3.369								
ν_{17}	198	208	0.228	0.012								
ν_{18}	110	122	3.250	5.032								
ν_{19}	47	55	0.135	0.027								

Notes. [a]Energy in units of cm^{-1}. [b]IR intensity in units of km mol^{-1}. [c]The two methods of calculation (MP2 and B3LYP) employ cc-pVTZ as the basis set and include the anharmonic corrections.

of HC_9N. As is usually observed for linear molecules, the values of q_v^e obtained by these calculations are slightly lower than the corresponding experimental values. Finally, Table B.4 collects the energies and intensities of the fundamental bands of all the vibrational modes of HC_5N, HC_7N, and HC_9N calculated at the MP2 and B3LYP levels of theory.